

# A Digital Twin of Synchronized Circular Laser Array for Powder Bed Fusion Additive Manufacturing

Hamed Attariani

Shayna Renay Petitjean

Majid Dousti (✉ [dousti.2@wright.edu](mailto:dousti.2@wright.edu))

Wright State University <https://orcid.org/0000-0002-2453-2787>

---

## Research Article

**Keywords:** Digital twin, Laser powder bed fusion, Synchronized multi-beam laser, Melt pool, Process variables, Microstructure, Ti-6Al-4V.

**Posted Date:** June 23rd, 2022

**DOI:** <https://doi.org/10.21203/rs.3.rs-1754427/v1>

**License:**   This work is licensed under a Creative Commons Attribution 4.0 International License.

[Read Full License](#)

---

# Abstract

The formation of undesirable microstructures and defects hinders the widespread use of additive manufacturing, e.g., the formation of columnar grains in Ti-6Al-4V leads to undesirable anisotropic mechanical properties. Here, the microstructure produced by a novel synchronized circular laser array for application in the powder bed fusion technique is investigated. The temporal temperature distribution for different process parameters (laser power, scanning speed, and internal distance between lasers in the array) were obtained by an anisotropic heat transfer model, and the Hunt criterion was employed to construct the solidification map. The results revealed that a degree of overlap between lasers is recommended to form a coherent melt pool, avoid degeneracy in surface quality, and maintain adequate resolution for all processing windows. However, laser overlap is not required for low scanning speed and high power scenarios. Finally, microstructure prediction shows that 45% of printed track includes equiaxed grains at a high power regime (500 W). However, the volume fraction of the equiaxed microstructure is reduced by decreasing laser power.

## 1. Introduction:

Additive manufacturing (AM) is executed through a layer-by-layer material deposition from a digital model. AM enables the production of complex components and devices [1, 2] with a diverse set of materials [3]. Among various AM techniques, considerable attention has been paid to the laser sintering technique, e.g., directed energy deposition (DED) [4, 5] and laser powder bed fusion (LPBF) [6, 7], for rapid prototyping of metals and ceramics. The laser melts and fuses the powder material layer by layer to form a three-dimensional object. The quality of the final product is highly dependent on material, powder, and laser speed/power/radius [8, 9]. Also, the final microstructure of parts differs from conventional manufacturing methods [10, 11]. For example, the columnar  $\beta$  grains are formed across the build's height in LPBF, leading to anisotropic mechanical behavior [12]. Additionally, the appearance of the  $\alpha'$  phase (fine acicular martensite) in the microstructure lowers the ductility of the printed part. Therefore, tremendous research studies have focused on techniques to control the microstructure toward forming the preferred equiaxed grain structure. Recently, the application of multi-laser powder bed fusion (MLPBF) has gained attraction due to its potential to alter the material's microstructure/properties and control the residual stress.

A computational study in [13] showed that adding an in-line or lateral second beam decreases thermal gradients and consequently reduces residual stresses [14]. Also, using two to four lasers decreased the residual stress on the top surface (up to  $\sim 17.93\%$ ) and increased the residual stress in the bottom center (up to  $\sim 80\%$ ) [15], i.e., the residual stress affects the likelihood of crack formation in LPBF. The numerical simulation of four laser arrays showed the dependency of the anisotropy of residual stress on the scanning strategy [16]. Moreover, the part distortion was reduced by 7.5% using a dual laser array with a lateral offset; the second beam is dedicated to the post-heating [17].

The experimental results of the dual scanning strategy with a slight coaxial offset showed a meaningful improvement in the maximum bending strength [18], although a multi-laser scanning technique showed no unwanted effect on the creep response of Inconel [19]. The experimental studies of M-LPBF showed the defect formation in the overlapped region and a lack of drastic change in the microhardness and tensile strength [20, 21]. Also, the Rosenthal solution was adopted for two coordinated heat sources [22]. The results showed a 20% increase in the melt pool depth and a 15% increase in melt pool length, but the change in the thermal gradients and microstructure was negligible. Finally, the post-treatment with the second laser in [23] formed a more uniform microstructure but did not alter the columnar microstructure. Among all existing experimental and numerical studies, a detailed study on the effect of a coordinated multi-laser array on microstructure is still lacking. Therefore, the main objective of this study is to employ MLPBF to alter microstructure. Finite element analysis (FEA) was used to calculate the solidification map for a circular laser array with constant laser spacing and investigate its promise to control the microstructure toward forming preferable equiaxed grains.

## 2. Computational Model:

The MOOSE (Multi-physics Object-Oriented Simulation Environment)[24] software was used to solve the anisotropic heat conduction equation. The model provides the temporal and spatial temperature distribution in a Ti-6Al-4V sample as the model material and obtains melt pool dimensions, solidification rate, and thermal gradient. The anisotropic thermal model has been widely used to model LPBF-AM due to its simplicity, low computational cost, and good agreement with experimental results [25–28]. The lists of equations, variables, and thermo-physical properties are in the Supplementary material, Table S1-3. The powder bed dimensions are 5×1.5×1.5 mm for high power and low-velocity scenario ( $P = 500$  W and  $v = 100$  mm/s) and 3×1.5×1.5 mm for the rest of the simulations. eight-node hexahedral elements with dimensions of 3×3×3  $\mu\text{m}$  were employed to mesh the simulation domain. The laser power and velocity range, Table 1, were selected to avoid the keyholing scenario [29]. All model parameters and laser characteristics are summarized in Table 1.

Table 1  
Model parameters for MLPBF-AM of Ti-6Al-4V [30].

| Parameter  | Notation                          | Value      |
|--|-----------------------------------|------------|
| Solidus Temperature (K)                                    | $T_S$                             | 1878       |
| Liquidus Temperature (K)                                   | $T_L$                             | 1993       |
| Melting Temperature (K)                                    | $T_m$                             | 1923       |
| Absorption Coefficient                                     | $A$                               | 0.25       |
| Laser Beam Radius ( $\mu\text{m}$ )                        | $r_o$                             | 75         |
| Laser Power (W)  | $P$                               | 50,300,500 |
| Laser Speed (mm/s)   | $v$                               | 100–1000   |
| Melting enthalpy (kJ/kg)                                   | $H_f$                             | 370        |
| Thermal conductivity enhancement factors                   | $\lambda_x, \lambda_y, \lambda_z$ | 10,10, 15  |
| Heat transfer convection ( $\text{W}/\text{m}^2\text{K}$ ) | $h_c$                             | 50         |
| Heat transfer radiation ( $\text{W}/\text{m}^2\text{K}$ )  | $h_r$                             | 1          |

Figure 1f illustrates the circular laser configuration consisting of five lasers with internal distancing  $r$ . The heat flux of each laser follows the Gaussian distribution, and the array's laser profile for  $P=300$  W, beam radius of  $75 \mu\text{m}$ , and various internal laser spacings,  $r=50-250 \mu\text{m}$ , is shown in Fig. 1a-e. The high-intensity heat flux occurs at the small spacing, and it reduces with an increase in  $r$ . It is worth noting that the overall shape of heat flux at the surface is controlled by  $r$ , e.g., a star-shaped heat profile is generated at  $r=75 \mu\text{m}$ , Fig. 1b. The laser power and speeds in the array are identical, and the internal spacing among lasers was kept constant during each simulation.

### 3. Results And Discussions:

**Model Verification** – The anisotropic heat transfer model was verified against a single laser's experimental melt pool dimensions due to the lack of experimental studies on the synchronized laser array. Figure 2 shows the model's melt pool width/height against the experimental results [27]. There is a good agreement between predicted and experimental depth. However, the model overestimates the width. The maximum 18.3% deviation in width is acceptable due to model and experimental uncertainties, i.e., the temperature dependence of laser absorption coefficient [31] and thermal conductivity enhancement factors, variation of density and thermal conductivity with powder porosity [26], and different possible mathematical equations for modeling laser-beam heat sources [28].

Melt Pool Prediction and Solidification Map – The solidification maps for all processing parameters, e.g., scanning speed, laser power, and internal spacing, are plotted in Fig. 3. The equations for thermal gradient ( $G$ ) and solidification rate ( $R$ ) were summarized in the supplementary material, Table S2. A 50 W laser results in columnar microstructure (Fig. 3a), i.e., the typical microstructure of LPBF-AM. However, raising the power to 300–500 W moves the  $G$ - $R$  lines toward the right-hand side of the solidification map, accompanied by the appearance of equiaxed grains in the printed track, Fig. 3b-c. Therefore, any further increase in power is expected to increase the equiaxed portion of the track; however, it may result in keyholing. In all modeled scenarios, increasing the scanning speed increases the  $R \times G$  value, indicating a grain size reduction. Also, more uniform grain size is expected in the high scanning speed regime for  $P=300\text{--}500$  W, i.e., the ( $G, R$ ) points conform better to constants  $R \times G$  lines. Figures 4–6 illustrate the melt pool shape and dimensions (width and depth) for all processing parameters.

The heat flux of each laser in the array contributes to the overall melting pool shape/dimensions based on their internal spacings, i.e., it is based on the superposition principle and thermal cross-talk among the temperature field of each laser. Generally, the width increases by increasing internal spacing distance due to heat distribution over a larger surface area, although the depth shows an opposite trend, i.e., it shows a decrease in heat penetration into the powder bed. Also, melt pool dimensions (depth and width) are decreased by increasing scanning velocity due to reducing laser-matter interaction time at high scanning speeds, which agrees with experimental and numerical studies of the single laser case [27]. It is worth noting that the dimensions of the discrete melt pool are not shown in Figures 4-6b because forming an incoherent melt pool is not desirable due to potential technical issues such as reducing surface quality and unwanted remelting from adjacent printing track. For example, four separate melt pools are formed for  $P=50$  W,  $v=100$  mm/s, and  $r=250$   $\mu\text{m}$  case, Figure 4a; in this scenario, the thermal cross-talk among lasers causes a higher temperature in the back laser melt pool than in the others. Therefore, the back laser dominates the melting, and the two sides' lasers only remelt the existing printed track. Also, an irregular melt shape appears for intermediate internal spacing ( $P=50$  W,  $v=100$  mm/s, and  $r=150$   $\mu\text{m}$ ), potentially creating issues at the printing edges. A similar trend for high laser powers ( $P=300\text{--}500$  W) was also observed, Figure 5-6. Generally, a degree of overlap among lasers ( $r \geq 150$   $\mu\text{m}$ ) is recommended to obtain a coherent melt pool shape and avoid any degradation in surface quality or dimensional inaccuracy at the edges. However, a high-power laser (500 W) with a slow-scanning speed (100 mm/s) increases the critical internal spacing to 250  $\mu\text{m}$  for obtaining a coherent melt pool, Figure 6a. Therefore, by pushing the laser power beyond  $P=500$  W and using a low scanning speed,  $v=100$  mm/s, the critical internal spacing can go beyond 250  $\mu\text{m}$ . Note that this is accompanied by increases in melt pool width and a reduction in printing resolution. Finally, the melt pool shapes for all processing parameters on the symmetric plane ( $x$ - $z$ ) and the top surface ( $x$ - $y$ ) are depicted in Figures S1-3 in the supplementary document.

Microstructure Prediction - The Hunt criterion [32] was employed to identify various microstructural zones (columnar, equiaxed, and mixed) on the liquidus line, i.e., columnar:

$G^{1.91} / R > 1.92 \times 10^6 K^{1.91} / cm^{2.91} . s$  and equiaxed:  $G^{1.91} / R < 1.04 \times 10^6 K^{1.91} / cm^{2.91} . s$ . The projection of critical  $G^{1.91} / R$  lines for each microstructural zone on the  $y$ - $z$  plane are illustrated in Fig. 7

for some representative cases. The enclosed area by each critical line was used to approximate the volume fraction of each microstructural zone. Figure 8 shows the columnar and equiaxed volume fractions for  $P=300\text{--}500\text{ W}$  at various scanning speeds and internal spacings. It is worth noting that the volume fraction of irregular/incoherent melt pool shapes was omitted from Fig. 8. The microstructure of side lasers, Fig. 7b, is predominantly mixed or columnar for irregular/incoherent melt pools. Therefore, the side lasers remelt and alter the microstructure back to the columnar in the second printing track. Figure 8 shows that the equiaxed volume fraction increases by increasing power. Also, the equiaxed volume fraction is more sensitive to scanning velocity variation at intermediate power ( $P=300\text{ W}$ ), i.e., the volume fraction increases from 20% for  $v=100\text{ mm/s}$  to 35.1% for  $v=500\text{ mm/s}$ ; however, this increase is only 4.62% for  $P=500\text{ W}$ . The interplay between velocity and power on absorbed heat can justify the decrease in velocity sensitivity by increasing power. In the low power regime, the scanning velocity becomes dominant, although, in the high-power regime, the power dominates the effect of velocity on  $R$  and  $G$  values and consequently on microstructure. The same trend is deduced for the internal spacing. The equiaxed volume fraction is reduced by increasing the internal spacing in a low power regime, although the distance between lasers in the array has a minor influence on the volume fractions in the high-power regime. The high power and the low velocity with a degree of overlap among lasers is recommended as the optimum processing window for the synchronized circular laser array. This setting can provide a coherent melt pool, adequate resolution, and a large volume fraction of the equiaxed microstructure.

## 4. Conclusion:

The final microstructure of Ti-6Al-4V alloy via a novel synchronized laser array was predicted for various processing parameters, such as scanning speed, laser power, and internal laser spacing. The results recommend using some overlap between lasers for low and intermediate laser powers (50–300 W) to form a continuous melt pool. However, overlap is not required in the high power scenario (500 W). Also, the best processing windows to maximize the equiaxed volume fraction is high power and low scanning velocity regime. In the high power regime, the equiaxed volume fraction is less sensitive to scanning speed and internal spacing. Further experimental studies should be conducted to verify these numerical predictions and also investigate the possibility of this approach to reducing residual stress.

## Declarations

### Acknowledgments:

The support of Wright State University is gratefully acknowledged, and the authors extend their special thanks to Dr. Mikhail Vorontsov for the initial discussions.

**Funding:** The Ohio Super Computing (OSC) computational grant, Grant No. ECS- PWSU0463.

**Conflicts of Interest/Competing Interests:** The authors declare no competing interests.

**Availability of Data and Material:** The datasets used or analyzed during the current study are partially available from the corresponding author on reasonable request.

**Code Availability:** The code is partially available from the corresponding author on reasonable request.

**Ethics Approval:** Not applicable

**Consent to Participate:** Not applicable.

**Consent for Publication:** Written informed consent for publication was obtained from all participants.

## References

1. Gaikwad AM, Steingart DA, Nga Ng T et al (2013) A flexible high potential printed battery for powering printed electronics. *Appl Phys Lett* 102. <https://doi.org/10.1063/1.4810974>
2. Ready S, Endicott F, Whiting GL et al (2013) 3D Printed Electronics
3. Kokkinis D, Schaffner M, Studart AR (2015) Multimaterial magnetically assisted 3D printing of composite materials. *Nat Commun* 6. <https://doi.org/10.1038/ncomms9643>
4. Babuska TF, Krick BA, Susan DF, Kustas AB (2021) Comparison of powder bed fusion and directed energy deposition for tailoring mechanical properties of traditionally brittle alloys. *Manuf Lett* 28:30–34. <https://doi.org/10.1016/j.mfglet.2021.02.003>
5. Bandyopadhyay A, Heer B (2018) Additive manufacturing of multi-material structures. *Mater Sci Eng R: Rep* 129:1–16
6. Wen S, Liu Y, Zhou Y et al (2021) Effect of Ni content on the transformation behavior and mechanical property of NiTi shape memory alloys fabricated by laser powder bed fusion. *Opt Laser Technol* 134. <https://doi.org/10.1016/j.optlastec.2020.106653>
7. Huang S, Sing SL, de Looze G et al (2020) Laser powder bed fusion of titanium-tantalum alloys: Compositions and designs for biomedical applications. *J Mech Behav Biomed Mater* 108. <https://doi.org/10.1016/j.jmbbm.2020.103775>
8. Wang DW, Zhou YH, Yao XY et al (2022) Inheritance of microstructure and mechanical properties in laser powder bed fusion additive manufacturing: A feedstock perspective. *Mater Sci Eng A* 832. <https://doi.org/10.1016/j.msea.2021.142311>
9. Kusuma C, The Effect of Laser Power and Scan Speed on Melt Pool The Effect of Laser Power and Scan Speed on Melt Pool Characteristics of Pure Titanium and Ti-6Al-4V Alloy for Selective Laser Melting
10. Bian L, Thompson SM, Shamsaei N (2015) Mechanical Properties and Microstructural Features of Direct Laser-Deposited Ti-6Al-4V. *JOM* 67:629–638
11. Cao S, Chen Z, Lim CVS et al (2017) Defect, Microstructure, and Mechanical Property of Ti-6Al-4V Alloy Fabricated by High-Power Selective Laser Melting. *JOM* 69:2684–2692
12. Shamsaei N, Yadollahi A, Bian L, Thompson SM (2015) An overview of Direct Laser Deposition for additive manufacturing; Part II: Mechanical behavior, process parameter optimization and control. *Additive Manuf* 8:12–35

13. Heeling T, Wegener K (2016) Computational investigation of synchronized multibeam strategies for the selective laser melting process. *Physics Procedia*. Elsevier B.V., pp 899–908
14. Sanchez S, Hyde CJ, Ashcroft IA et al (2021) Multi-laser scan strategies for enhancing creep performance in LPBF. *Additive Manuf* 41. <https://doi.org/10.1016/j.addma.2021.101948>
15. Chen C, Xiao Z, Zhu H, Zeng X (2020) Distribution and evolution of thermal stress during multi-laser powder bed fusion of Ti-6Al-4 V alloy. *J Mater Process Technol* 284. <https://doi.org/10.1016/j.jmatprotec.2020.116726>
16. Masoomi M, Thompson SM, Shamsaei N (2017) Laser powder bed fusion of Ti-6Al-4V parts: Thermal modeling and mechanical implications. *Int J Mach Tools Manuf* 118–119:73–90. <https://doi.org/10.1016/j.ijmachtools.2017.04.007>
17. Gerstgrasser M, Cloots M, Stirnimann J, Wegener K Residual stress reduction of LPBF-processed CM247LC samples via multi laser beam strategies. <https://doi.org/10.1007/s00170-021-07083-6/Published>
18. Abe F, Osakada K, Shiomi M et al The manufacturing of hard tools from metallic powders by selective laser melting
19. Sanchez S, Hyde CJ, Ashcroft IA et al (2021) Multi-laser scan strategies for enhancing creep performance in LPBF. *Additive Manuf* 41. <https://doi.org/10.1016/j.addma.2021.101948>
20. Zhang C, Zhu H, Hu Z et al (2019) A comparative study on single-laser and multi-laser selective laser melting AlSi10Mg: defects, microstructure and mechanical properties. *Mater Sci Eng A* 746:416–423. <https://doi.org/10.1016/j.msea.2019.01.024>
21. Wei K, Li F, Huang G et al (2021) Multi-laser powder bed fusion of Ti–6Al–4V alloy: Defect, microstructure, and mechanical property of overlap region. *Mater Sci Eng A*. <https://doi.org/10.1016/j.msea.2020.140644>. 802:
22. Evans R, Gockel J Modeling the effects of coordinated multi-beam additive manufacturing. <https://doi.org/10.1007/s00170-021-07279-w/Published>
23. Reza Ansari Dezfoli A, Hwang W-S, Huang W-C, Tsai T-W (2017) Determination and controlling of grain structure of metals after laser incidence: Theoretical approach. *Nat Publishing Group*. <https://doi.org/10.1038/srep41527>
24. Xie Z, Jiang W, Wang C, Wu X (2021) Bayesian Inverse Uncertainty Quantification of a MOOSE-based Melt Pool Model for Additive Manufacturing Using Experimental Data
25. Kamara AM, Wang W, Marimuthu S, Li L (2011) Modelling of the Melt Pool Geometry in the Laser Deposition of Nickel Alloys Using the Anisotropic Enhanced Thermal. 87–99. <https://doi.org/10.1177/09544054JEM2129>. Conductivity Approach: <https://dx.doi.org/10.1177/09544054JEM2129> 225
26. Yang J, Sun S, Brandt M, Yan W (2010) Experimental investigation and 3D finite element prediction of the heat affected zone during laser assisted machining of Ti6Al4V alloy. *J Mater Process Technol* 210:2215–2222. <https://doi.org/10.1016/J.JMATPROTEC.2010.08.007>

27. Yin J, Peng G, Chen C et al (2018) Thermal behavior and grain growth orientation during selective laser melting of Ti-6Al-4V alloy. *J Mater Process Technol* 260:57–65. <https://doi.org/10.1016/J.JMATPROTEC.2018.04.035>
28. Zhang Z, Huang Y, Rani Kasinathan A et al (2019) 3-Dimensional heat transfer modeling for laser powder-bed fusion additive manufacturing with volumetric heat sources based on varied thermal conductivity and absorptivity. *Opt Laser Technol* 109:297–312. <https://doi.org/10.1016/J.OPTLASTEC.2018.08.012>
29. Patel S, Vlasea M (2020) Melting modes in laser powder bed fusion. *Mater (Oxf)* 9:100591. <https://doi.org/10.1016/J.MTLA.2020.100591>
30. TOULOUKIAN SY (1970) Thermal conductivity, Nonmetallic Solids. *Thermophys Prop Matter* 2:183–193
31. Unni AK, Vasudevan M (2021) Determination of heat source model for simulating full penetration laser welding of 316 LN stainless steel by computational fluid dynamics. *Materials Today: Proceedings* 45:4465–4471. <https://doi.org/10.1016/J.MATPR.2020.12.842>
32. Kobryn PA, Semiatin SL (2003) Microstructure and texture evolution during solidification processing of Ti–6Al–4V. *J Mater Process Technol* 135:330–339. [https://doi.org/10.1016/S0924-0136\(02\)00865-8](https://doi.org/10.1016/S0924-0136(02)00865-8)

## Figures

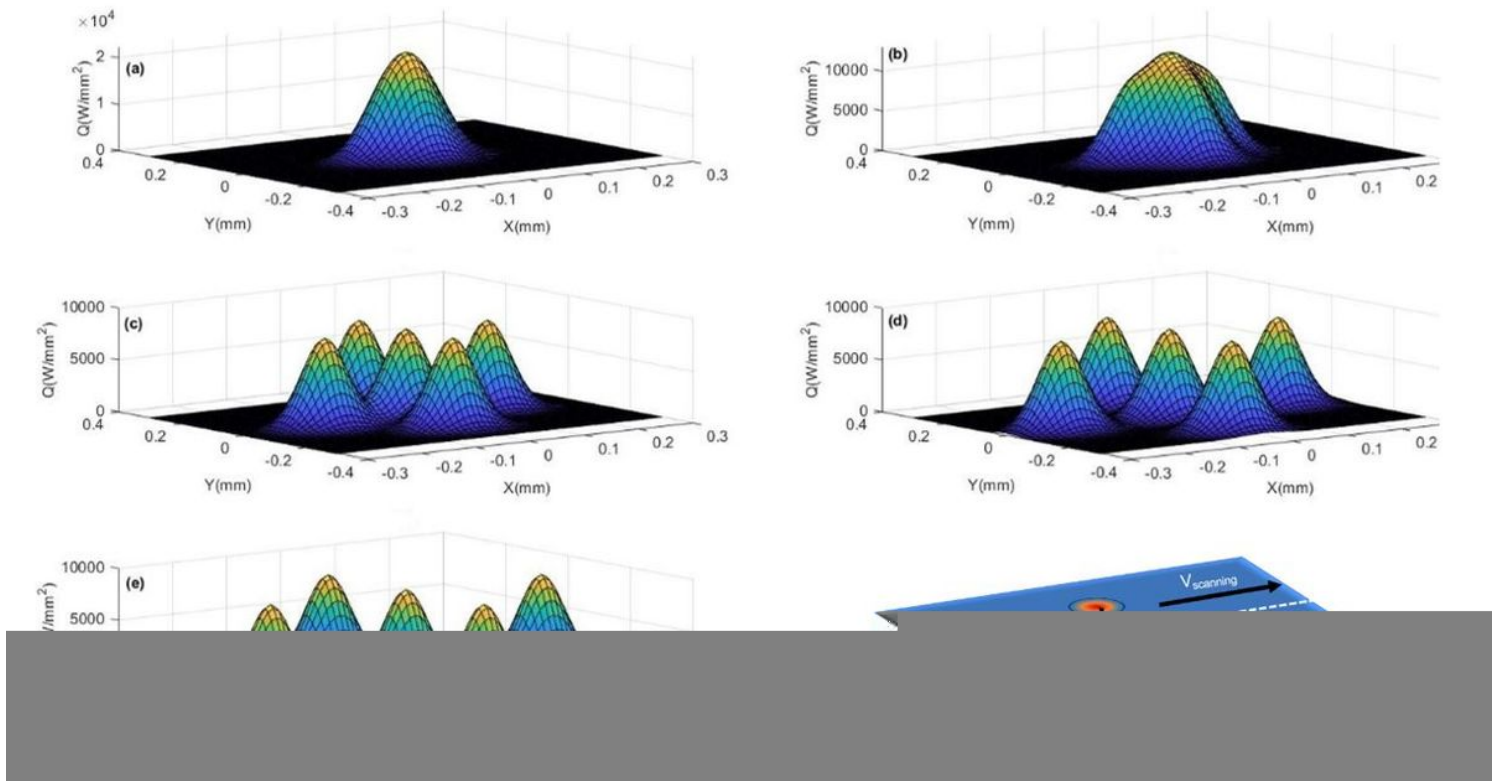


Figure 1

The laser heat flux for  $P=300$  W and various internal laser distances,  $r$ . a)  $r=50$   $\mu\text{m}$ , b)  $r=75$   $\mu\text{m}$ , c)  $r=150$   $\mu\text{m}$ , d)  $r=200$   $\mu\text{m}$ , and e)  $r=250$   $\mu\text{m}$ . f). The schematic of the circular laser array. The distance between laser spots is designated by  $r$ , and it is constant during scanning.

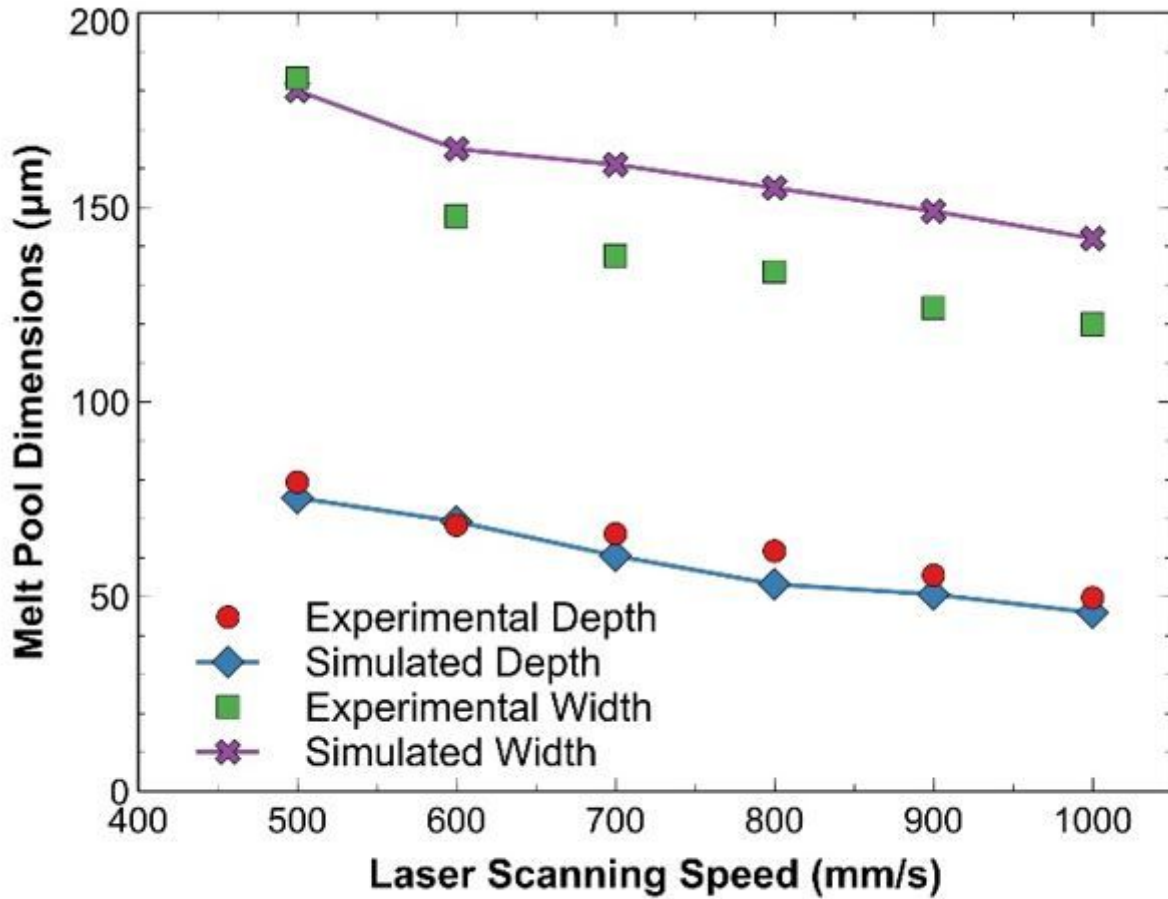
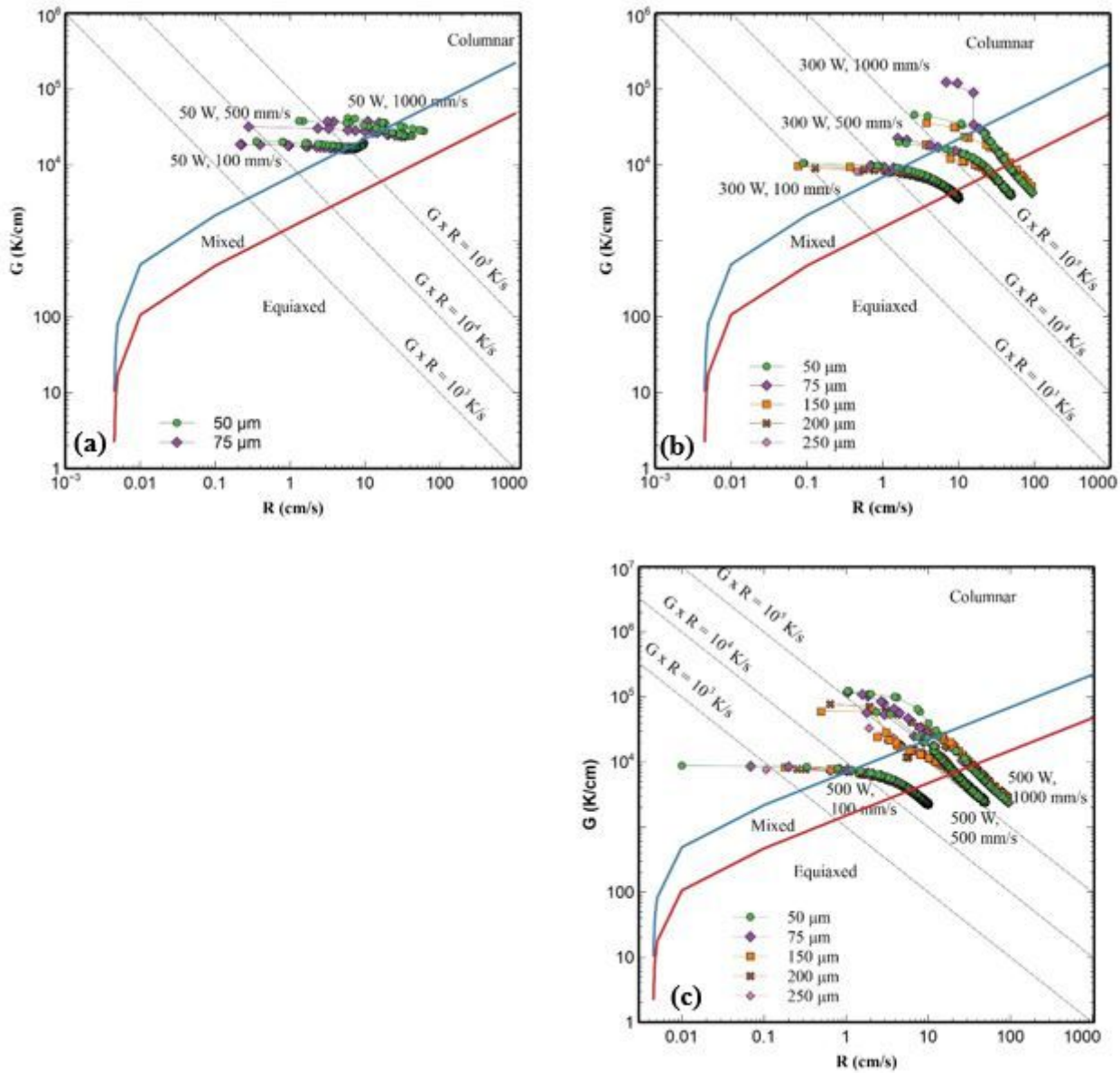


Figure 2

The experimental and numerical melt pool dimensions. The laser power (300 W) and laser beam radius ( $75$   $\mu\text{m}$ ) are identical to the experimental setup [27].



**Figure 3**

The solidification map for the various process parameters. a)  $P=50$  W and  $v=100$ - $1000$  mm/s. b)  $P=300$  W and  $v=100$ - $1000$  mm/s. c)  $P=500$  W and  $v=100$ - $1000$  mm/s.

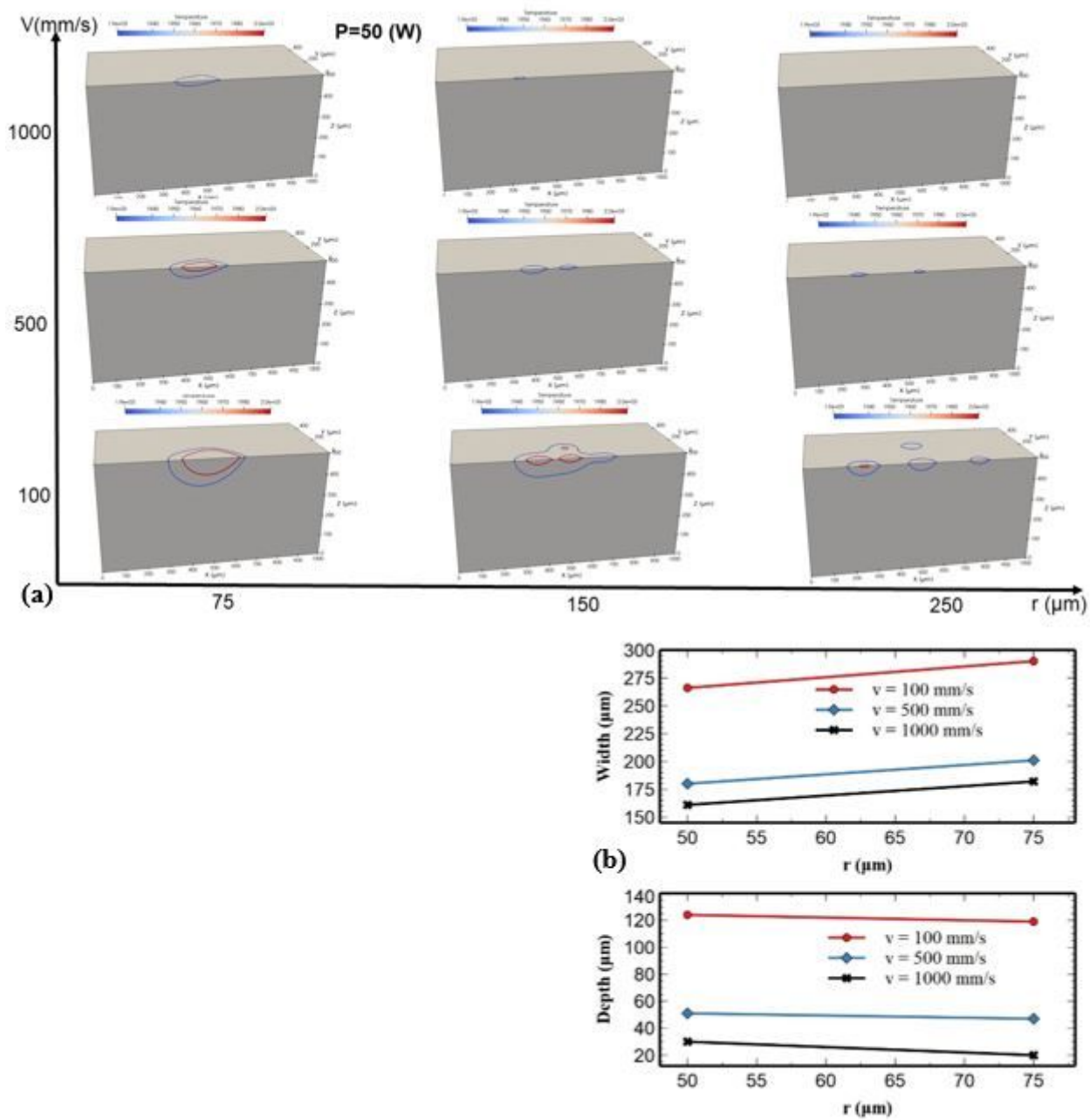
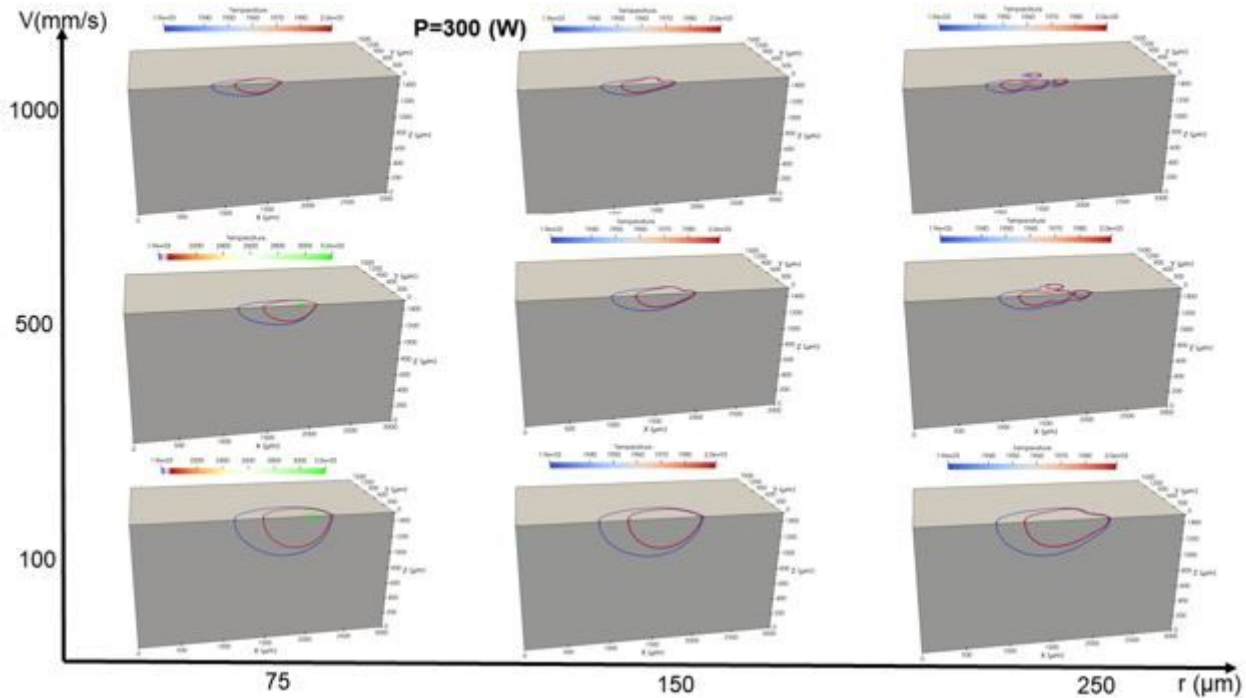
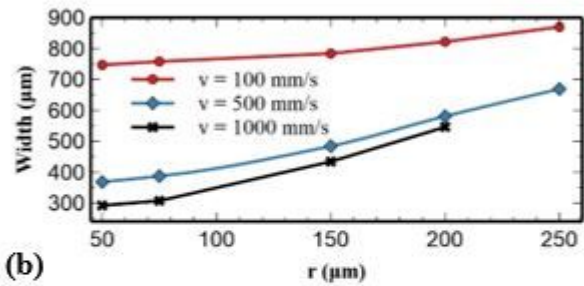


**Figure 4**

Melt pool shape, width, and depth, for various processing parameters (beam velocity and internal laser distancing) at the constant power scenario ( $P=50$  W). a) The melt pool shape for different velocity sets and internal laser distancing. The red contour presents the liquidus temperature ( $T_D$ ), and the blue line identifies the melting temperature ( $T_M$ ). b) The melt pool width and depth for  $P=50$  W.



(a)



(b)

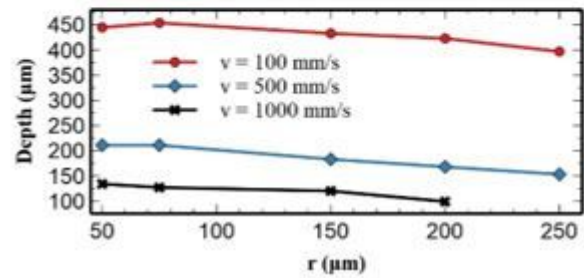
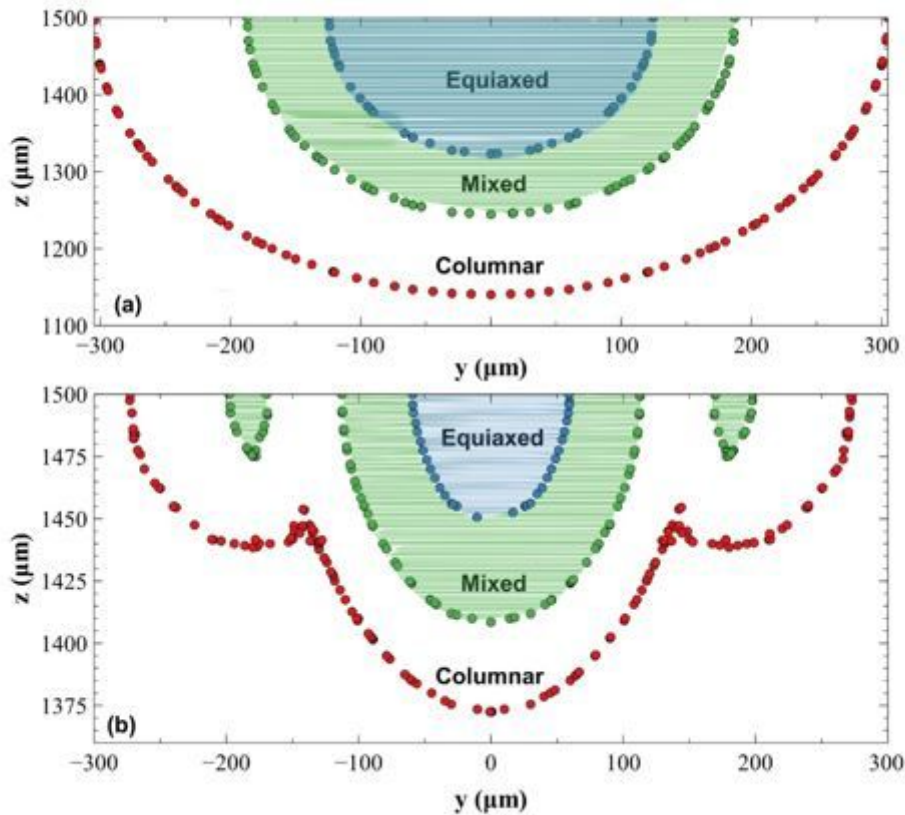


Figure 5

Melt pool shape, width, and depth for various processing parameters (beam velocity and internal laser distancing) at the constant power scenario ( $P=300\text{ W}$ ). a) The melt pool shape for different scanning velocity sets and internal laser distancing. The red contour presents the liquidus temperature ( $T_L$ ), the blue line identifies the melting temperature ( $T_M$ ), and the green line represents the evaporation temperature ( $T_E$ ). b) The melt pool width and depth for  $P=300\text{ W}$

Figure 6

Melt pool shape, width, and depth, for various processing parameters (beam velocity and internal laser distancing) at the constant power scenario ( $P=500$  W). a) The melt pool shape for different velocity sets and internal laser distancing. The red contour presents the liquidus temperature ( $T_L$ ), the blue line identifies the melting temperature ( $T_M$ ), and the green represents the evaporation temperature ( $T_E$ ). b) The melt pool width and depth for  $P=500$  W.



**Figure 7**

The projection of critical  $G^{191}/R$

values into the y-z plane that passes through the deepest point of the melt pool for two representative cases, i.e., regular vs. irregular. The red line identifies the liquidus line. The green and blue lines represent the Hunt criterion for mixed and equiaxed regions. a)  $P=300$  W,  $v=100$  mm/s, and  $r=50$   $\mu\text{m}$ . b)  $P=300$  W,  $v=500$  mm/s, and  $r=200$   $\mu\text{m}$ .

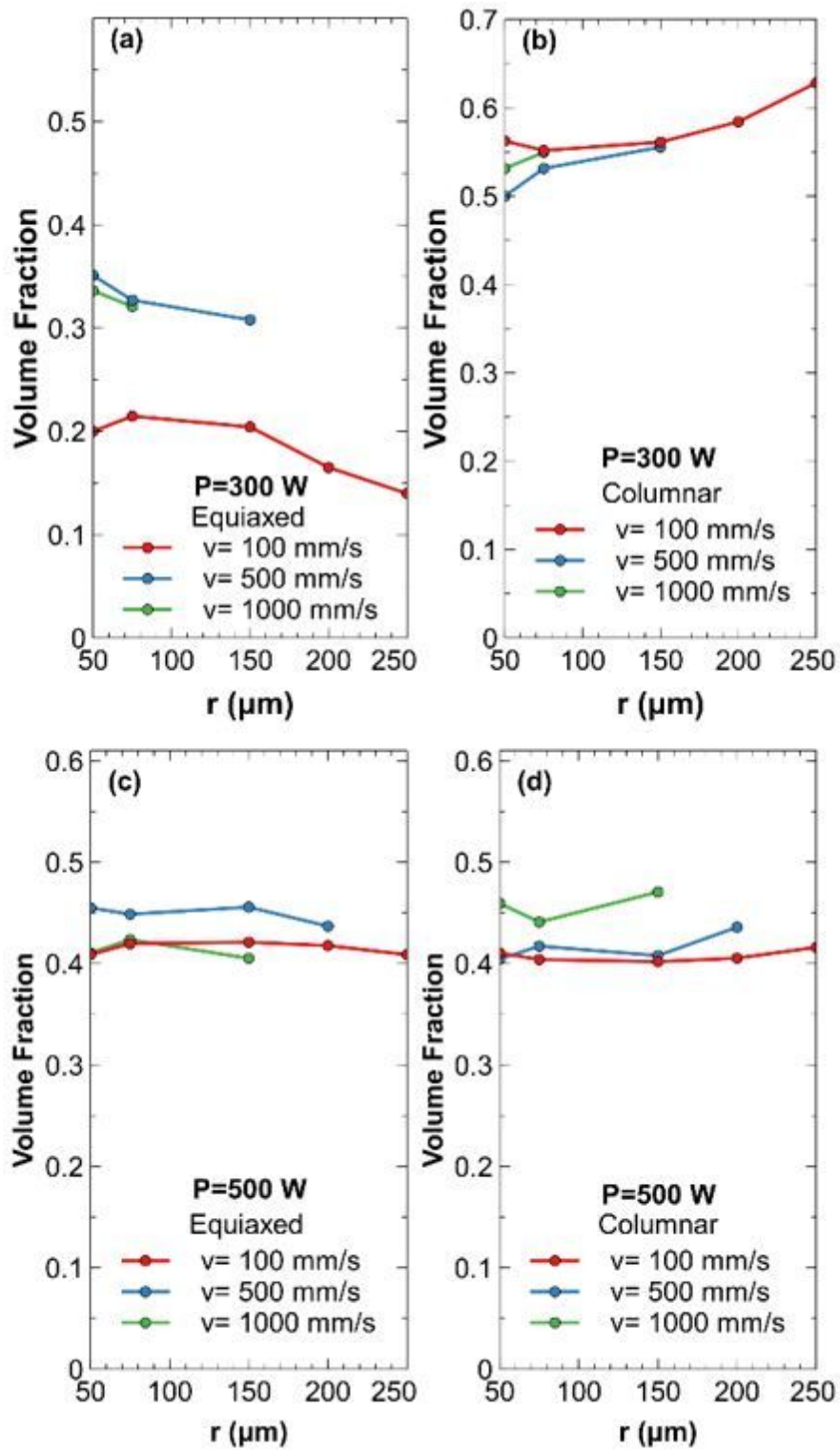


Figure 8

The volume fraction of equiaxed and columnar microstructure for  $P=300-500$  W,  $v=100-1000$  mm/s, and  $r=50-250$   $\mu\text{m}$ .

## Supplementary Files

This is a list of supplementary files associated with this preprint. Click to download.

- [MultiBeamLaserAMSupp.docx](#)